Soft Matter

PAPER

View Article Online
View Journal | View Issue

Cite this: *Soft Matter*, 2024, 20, 9007

Scale-dependent interactions enable emergent microrheological stress response of actin–vimentin composites†

Julie Pinchiaroli,[a] Renita Saldanha,[b] Alison E. Patteson,[b] Rae M. Robertson-Anderson [c] and Bekele J. Gurmessa *[a]

Received 16th August 2024,
Accepted 28th October 2024

DOI: 10.1039/d4sm00988f

rsc.li/soft-matter-journal

The mechanical properties of the mammalian cell regulate many cellular functions and are largely dictated by the cytoskeleton, a composite network of protein filaments, including actin, microtubules, and intermediate filaments. Interactions between these distinct filaments give rise to emergent mechanical properties that are difficult to generate synthetically, and recent studies have made great strides in advancing our understanding of the mechanical interplay between actin and microtubule filaments. While intermediate filaments play critical roles in the stress response of cells, their effect on the rheological properties of the composite cytoskeleton remains poorly understood. Here, we use optical tweezers microrheology to measure the linear viscoelastic properties and nonlinear stress response of composites of actin and vimentin with varying molar ratios of actin to vimentin. We reveal a surprising, nearly opposite effect of actin–vimentin network mechanics compared to single-component networks in the linear *versus* nonlinear regimes. Namely, the linear elastic plateau modulus and zero-shear viscosity are markedly reduced in composites compared to single-component networks of actin or vimentin, whereas the initial response force and stiffness are maximized in composites *versus* single-component networks in the nonlinear regime. While these emergent trends are indicative of distinct interactions between actin and vimentin, nonlinear stiffening and long-time stress response appear to both be dictated primarily by actin, at odds with previous bulk rheology studies. We demonstrate that these complex, scale-dependent effects arise from the varied contributions of network density, filament stiffness, non-specific interactions, and poroelasticity to the mechanical response at different spatiotemporal scales. Cells may harness this complex behavior to facilitate distinct stress responses at different scales and in response to different stimuli to allow for their hallmark multifunctionality.

1 Introduction

The cytoskeleton of mammalian cells is comprised of three distinct filamentous proteins: actin, microtubules, and intermediate filaments (IFs). These filaments work together to provide cells with mechanical integrity while also regulating myriad mechanical processes such as cell adhesion, cell division, nuclear positioning, and migration.[1–7] Each of these filaments has distinct stiffness, size, and stability that dictate their different functions. More recently, it has become increasingly appreciated that interactions and crosstalk between the different filaments are equally critical to many mechanical processes.[8–13] Similarly, in materials applications, composites of polymers of varying stiffnesses are often employed to evade the limitations of single-component networks, allowing for emergent mechanical properties such as increased resilience and tunability.[9,12,14,15]

Semiflexible actin filaments and rigid microtubules are highly preserved in cells and well characterized, and their mechanical properties and cellular functions of their networks have been extensively investigated both *in vivo* and *in vitro*.[4,8,11] Conversely, intermediate filaments constitute an entire class of 50 different proteins, with each type having different structural and mechanical properties.[16–18] Even a single IF type, such as vimentin, which is expressed in mesenchymal cells and plays key roles in cell adhesion, migration, and mechanosensing,[19–23] can adopt a wide range of lengths and conformations and may non-specifically crosslink with neighboring IFs or other proteins.[8,18,24,25] This diversity allows IFs to contribute to many different cellular

[a] *Department of Physics and Astronomy, Bucknell University, Lewisburg, PA 17837, USA. E-mail: b.gurmessa@bucknell.edu*
[b] *Department of Physics and BioInspired Institute, Syracuse University, Syracuse, NY 13210, USA*
[c] *Department of Physics and Biophysics, University of San Diego, San Diego, CA 92110, USA*

† Electronic supplementary information (ESI) available. See DOI: https://doi.org/10.1039/d4sm00988f

functions and has in part obscured how their mechanical properties enable these different functionality in cells.[26] Nevertheless, previous studies have suggested that IFs are essential to the hallmark stress stiffening and recovery behavior of cells.[7,17,26–28] How these distinct mechanical features rely on or are impacted by the presence of the other cytoskeletal filaments remains poorly understood.

Here, we address this problem by determining the linear and nonlinear microrheological properties of composites of actin filaments and vimentin IFs with varying molar fractions of each component, revealing intriguing emergent mechanical properties that are highly dependent on the spatiotemporal strain characteristics. Semiflexible actin filaments, which play pivotal roles in cellular functions, ranging from tensile strength and apoptosis to motility and replication, have persistence lengths of $l_p \simeq 10$ μm, comparable to their typical contour lengths $L \approx 5$–20 μm.[1–4,29–31] *In vitro*, entangled networks of actin filaments exhibit linear viscoelastic properties that can be described by extensions of the reptation model to semiflexible polymers, with a low-frequency elastic plateau modulus that scales as $G^0 \quad c^{1.4}$.[32,33] The nonlinear response of entangled actin networks is more complex, with networks exhibiting varying degrees of stress stiffening and softening, as well as different relaxation mechanisms and timescales, depending on the spatiotemporal scale of the strain and the actin concentration.[34–40]

Vimentin forms a meshwork that envelops actin bundles and stress fibers in cells.[5,41] Vimentin IFs have similar contour lengths as actin filaments but are much more flexible, with $l_p \simeq 2$ μm.[16] They have been shown to be uniquely extensible, a feature which has been implicated in their excepted role in stress absorption, deformability, and stiffening of cells.[25,42–44] Reconstituted vimentin IF networks exhibit minimal stress relaxation in the linear regime, with linear viscoelastic moduli that display very weak scaling with frequency. The concentration dependence of G^0 has also been shown to be weaker than that for actin networks, with $G^0 \quad c^{0.47}$ reported for bulk rheology measurements.[20] Above a critical strain, vimentin networks exhibit stress stiffening that can be described as $K \quad \sigma^{3/2}$ where K is the nonlinear modulus and σ is stress.[45] Moreover, the degree of stiffening and critical stiffening strain are dependent on the concentration of vimentin and divalent salts.[21,25] Specifically, substantial stiffening has been attributed to crosslinking of VIFs by divalent cations, with subsequent yielding resulting from crosslink rupture.[21,22,46–48]

Despite their significance to cellular processes and materials applications, the mechanical properties of composites of actin and vimentin are not fully understood. Bulk rheological measurements have reported nonmonotonic dependence of the elastic modulus G' on the molar fraction of actin in the composite ϕ_A, reaching a pronounced peak at $\phi_A = 0.25$, which was attributed to non-specific crosslinking between actin and the tail-domain of vimentin.[18] Furthermore, bulk measurements on composites of actin and another IF, keratin, reported similar albeit weaker nonmonotonicity.[49] However, similar studies performed on actin–VIF composites at lower protein and salt concentrations reported a monotonic increase in G' with ϕ_A.[16] Theoretical models that recapitulated this monotonic trend incorporate non-specific interactions between vimentin IFs but no actin–vimentin interactions.[50] In response to nonlinear bulk strains, the addition of vimentin to crosslinked actin has been reported to either increase or decrease the degree of stress stiffening, dependent on the actin concentration.[9] These findings, captured by theoretical models, were shown to arise from the ability of vimentin to either suppress or enhance actin crosslinking, depending on the actin and crosslinker concentrations. Finally, particle-tracking microrheology experiments of VIF networks at fixed concentration with varying concentrations of actin added reported scaling $G_0 \quad c_A^{1.5}$,[51] similar but slightly larger than $G_0 \quad c_A^{1.4}$ reported for actin networks in the absence of VIFs.[52]

These few studies, reporting complex and conflicting results, underscore our limited understanding of the mechanics of actin–IF composites and the need for microscale and mesoscale rheology measurements that are equipped to delineate the various contributions to the varied bulk response features reported. For example, the extent to which VIFs non-specifically crosslink to each other or to neighboring actin filaments, and the mechanical properties that emerge from these interactions, remain topics of debate. Moreover, the extent to which actin–VIF composites exhibit stress-stiffening, softening or linear elasticity, as well as emergent mechanics *versus* monotonic trends, are important unanswered questions.

Here, to address these questions, we use optical tweezers microrheology to characterize the linear and nonlinear mechanical response of *in vitro* composites of co-entangled actin filaments and vimentin IFs (Fig. 1). We quantify the frequency-dependent viscoelastic moduli $G'(\omega)$ and $G''(\omega)$ from the thermal fluctuations of optically trapped microsphere probes embedded in the composites. We also further characterize the nonlinear response by optically displacing probes through the composites and measuring the forces the composites exert on the probes during and after the strain (Fig. 1(B)–(D)). We show that the dependence of rheological properties on composite composition (*i.e.*, fraction of actin ϕ_A) is markedly different in the linear and nonlinear regime as well as at different timescales. Namely, composites displayed reduced elastic moduli and zero-shear viscosity compared to single-component networks, while short-time nonlinear stress response and stiffness are enhanced in composites. These nearly opposite emergent behaviors suggest a careful interplay between network connectivity and filament rigidity, as well as the prevalence of easily disrupted IF interactions. Moreover, we demonstrate that the actin fraction dictates the long-time behavior and degree of stress-stiffening, at odds with current thought based on bulk rheology experiments. Our results suggest that cells may utilize this complex behavior to enable various stress responses at different scales and in reaction to various stimuli, allowing for their versatile functionality.

2 Materials and methods

Protein preparation

Rabbit skeletal actin (Cytoskeleton, Inc., AKL99) was reconstituted to 46 μM in G-buffer [2 mM Tris pH 8.0, 0.5 mM DTT, 0.1 mM $CaCl_2$, 0.2 mM ATP] and stored in single-use aliquots at

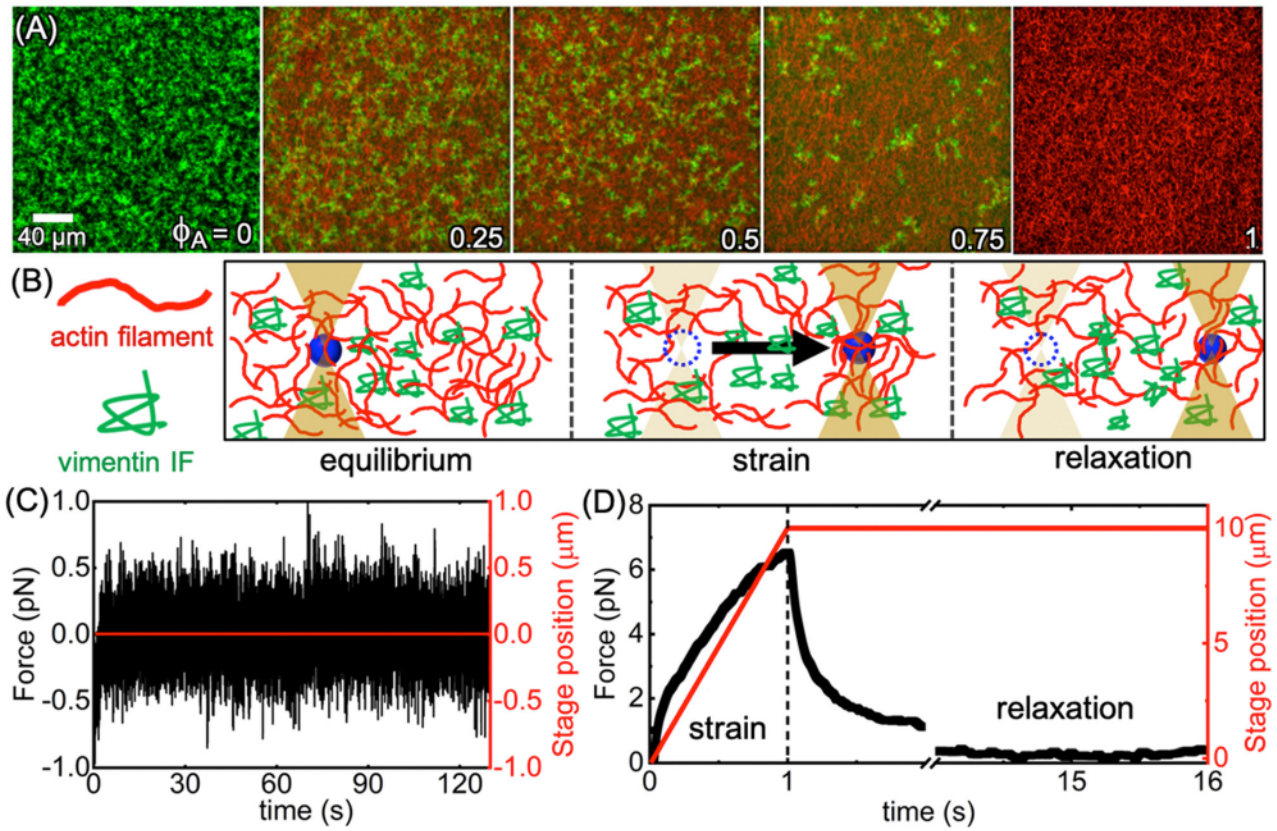

Fig. 1 Design and optical tweezers microrheology of entangled composites of actin filaments and vimentin intermediate filaments. (A) Composite networks of actin filaments (red) and vimentin intermediate filaments (green) prepared at fixed total protein concentration $c_A + c_V$ = 11.6 μM with varying molar fractions of actin $\phi_A = c_A/(c_A + c_V)$ = 0, 0.25. 0.5, 0.75 and 1 (left to right). Each image is a z-projection of a stack of 35 512 512 square-pixel images separated in z by 0.5 μm (see Fig. S1(A), ESI†), collected with a Leica TCS SP5 laser scanning confocal microscope with 63 1.4 NA objective. (B)–(D) Optical tweezers microrheology measurements of actin–vimentin composites. (B) Cartoon depicting a microsphere probe (blue) of diameter d = 4.2 μm embedded in an actin–vimentin composite and trapped by a focused laser beam during the three phases of an OTM experiment: (equilibrium) the probe is held fixed, (strain) the probe is displaced 10 μm through the composite at a constant speed of v = 10 μm s^{-1} by moving the sample stage relative to the trap, and (relaxation) the trap is held fixed following the strain as the probe relaxes back to the center of the trap. The force exerted on the probe during all phases is collected at 20 kHz. (C) The equilibrium phase is used to determine linear viscoelastic properties. For linear OTM measurements, the stage position (red) is held fixed, and the thermal force fluctuations (black) are measured for 130 s to extract frequency-dependent linear viscoelastic moduli $G'(\omega)$ and $G''(\omega)$. (D) For nonlinear OTM measurements, the force exerted on the probe (black) is measured during the strain and relaxation phases, during which the stage position (red) increases and is then held constant. Sample data shown in (C) and (D) are for the ϕ_A = 0.75 composite.

−80 C. Rhodamine phalloidin (Cytoskeleton, Inc., PHDR1) was reconstituted to 14 μM in methanol and stored at −20 C. Vimentin was prepared by expressing vimentin-coding DNA (pETE7 plasmid provided by Robert Goldman) in *Escherichia coli* BL21(DE3) component cells, as described previously.[53] Briefly, vimentin was isolated, pooled, dialyzed against a denaturing buffer [50 mM Tris–HCl (pH 8.5), 6 M urea], and flash-frozen for storage at −80 C. Samples were then dialyzed into a solution containing 5 mM Tris–HCl (pH 8.4) and 1 mM DTT, as described previously,[53,54] by gradually lowering the urea concentration in a step-wise fashion (6 M, 4 M, 2 M, 0 M) at room temperature (RT) for 20 min for every dialysis step except the final step which was performed overnight at 4 C.

Cell culture

Wild-type mouse embryonic fibroblasts (mEFs) were kindly provided by J. Ericsson (Abo Akademi University, Turku, Finland). Cells were maintained in Dulbecco's modified Eagle's medium (DMEM), including HEPES and sodium pyruvate supplemented with 10% fetal bovine serum (FBS), 1% penicillin–streptomycin, and non-essential amino acids. Cell cultures were maintained at 37 C with 5% CO_2.

Immunofluorescence

Cells were fixed for immunofluorescence using 4% paraformaldehyde (Fisher Scientific) for 30 minutes at 37 C. Cell membranes were permeabilized with 0.05% Triton-X (Fischer BioReagents) in PBS for 15 minutes at RT and blocked with 1% bovine serum albumin (BSA) for 1 hour at RT. For vimentin visualization, cells were incubated with primary rabbit anti-vimentin antibody (Abcam) diluted 1 : 200 in 1% BSA in PBS for 1.5 hours at RT; the secondary antibody anti-rabbit Alexa Fluor 647 (Invitrogen) was used at a dilution of 1 : 1000 in 1% BSA in PBS for 1 hour at RT. For visualizing actin filaments, cells were stained with rhodamine phalloidin 488 (Invitrogen) diluted 1 : 200 in 1% BSA in PBS and incubated for 1 hour at RT.

Actin–vimentin composite preparation

To prepare composites, actin and vimentin filaments were polymerized separately, then mixed and flowed into a microscope sample chamber assembled using double-sided tape as a spacer between a microscope slide and glass coverslip. Actin filaments were polymerized from actin monomers by incubating in an F-buffer [10 mM Imidazole pH 7.0, 50 mM KCl, 1 mM $MgCl_2$, 1 mM EGTA, 0.2 mM ATP] at RT for 1 h. Vimentin IFs were polymerized *via* the addition of 50 mM Na^+ and incubation at 37 C for 30 minutes. Under these conditions, the lengths of actin filaments and VIFs are expected to be $L_A \simeq 8 \pm 3$ μm and $L_V \simeq$ 5–10 μm, respectively.[35,41] To form the composite, the solution of polymerized actin was added to the solution of polymerized vimentin, which was then mixed slowly by pipetting up and down 10 times before introducing the composite solution into the sample chamber *via* capillary action. The open ends of the sample chamber were sealed with epoxy and the composites was allowed to equilibrate for 10–15 minutes before collecting data. All composites comprise the same total protein concentration of $c = c_A + c_V = 11.6$ μM with varying molar fractions of actin $\phi_A = c_A/(c_A + c_V) =$ 0, 0.25, 0.5, 0.75, 1 (Fig. 1(A)).

A trace amount of polystyrene microspheres (#FSDG006 dragon green, Bangs Laboratory, Inc.) of 4.2 μm in diameter was added for microrheology measurements. Microspheres are passivated with Tween-20 to prevent non-specific interactions with the filaments. The probe interface can thus be considered a no-stick slip boundary. Moreover, the bead size was chosen to be substantially larger than the mesh size of the composites to ensure that our results are not complicated by non-continuum effects and reduced local viscosity.[55,56]

In vitro imaging

To determine the structure of the interpenetrating networks of actin filaments and VIFs in composites, a Leica TCS SP5 laser scanning confocal microscope with 63 1.4 NA objective was used to image fluorescent-labeled actin and vimentin filaments within composites of the same concentration and ϕ_A values as in microrheology experiments (Fig. 1(A)). Acti-Stain 555 Phalloidin (Cytoskeleton, Inc) was used to label actin filaments and Alexa Fluor 488 maleimide (Invitrogen) was used to covalently label vimentin, as described in ref. 57. To reduce photobleaching, oxygen scavenging agents (4.5 μg ml^{-1} glucose, 0.005% β-mercaptoethanol, 4.3 μg ml^{-1} glucose oxidase, 0.7 μg ml^{-1} catalase) were included. Stacks of 35 images, each 512 512 square-pixels (246.5 246.5 μm) in area, with z step of 0.5 μm between imaging planes were collected. Each image shown in Fig. 1(A) is a mean intensity projection of a representative stack. Fig. S1(A) (ESI†) shows the corresponding single-channel stacks, temporally color-coded by z-height.

To determine structural correlation lengths for the two networks comprising the composites, spatial image autocorrelation (SIA) analysis was performed on each image of each z-stack using a custom-written Python script.[58–60] SIA measures the correlation in intensity $I(r)$ of two pixels in an image separated by any given radial distance r by taking the product of the fast Fourier transform F of an image I and its complex conjugate, applying an inverse Fourier transform F^{-1}, and then normalizing by the intensity squared: $g(r) = F^{-1}(|F(I(r))|^2)/[I(r)]^2$. The resulting autocorrelation $g(r)$ generally decays with increasing r, and the critical decay distance ξ_g is a measure of the average size of features in the image. For an image of a homogeneous network, ξ is often considered analogous to the mesh size. The correlation length ξ was determined from our data by fitting the exponentially decaying section of each autocorrelation curve to $g(r) = g_o \exp(-r/\xi)$, as described previously.[61,62]

In vivo imaging

The actin and vimentin samples were labeled with phalloidin 488 (Invitrogen) and Alexa Fluor 647 (Invitrogen) respectively. The images were captured using spinning disk confocal microscopy (Yokogawa CSU-W1) with an inverted Nikon Ti-E microscope and a 100 oil immersion objective (1.49 NA) imaged onto an Andor Zyla CMOS camera. Images shown in Fig. 2(A) are mean intensity projections of 20 z-stacks of 75 μm 100 μm with 15.4 pixels per μm.

Optical tweezers microrheology

All optical tweezers microrheology (OTM) measurements were performed using an optical trap built around an IX73 fluorescence microscope (Olympus, Melville, NY) with a 1064 nm Nd:YAG fiber laser (BKtel, RPMC Lasers, Inc) focused with a 60 1.42 NA oil immersion objective lens (UPLXAPO60XO 60 NA 1.42, Olympus). The force was measured using a position-sensing detector (PSM2-10Q PSD module coupled with amplifier OT-301, ON-TRAK Photonics, Inc) that recorded the deflection of the trapping laser, which is proportional to the force acting on the trapped probe. The trap stiffness, which relates the laser deflection to force, was measured using Stokes drag[56] and passive equipartition calibration methods.[63,64]

We performed average linear OTM measurements of 20 trials by 20 beads at 20 different locations in the sample by recording the thermal fluctuations of an optically trapped probe for 135 seconds at a frequency of 20 kHz. Because the probe is held fixed by the trap and only subject to thermal fluctuations of the surrounding filaments, it does not distort or perturb the network, a criterion for the linear response regime.

From this data, we extracted the storage modulus ($G'(\omega)$) and loss modulus ($G''(\omega)$) as a function of the angular frequency ω *via* the generalized Stokes–Einstein relation (GSER) as described in ref. 65. In brief, the normalized mean-squared displacement of the ensemble of trapped beads, $(\tau) = \dfrac{\langle \Delta r^2(\tau) \rangle}{2\langle r^2 \rangle}$, was computed, after which $\hat{}(\omega)$, the Fourier transform of (τ), was obtained *via* the relationship explained in Tassieri *et al.*:[65]

$$-\omega^2 \hat{}(\omega) = \frac{(\tau_1)}{\tau_1}\left(1 - e^{-i\omega\tau_1} + {}_{\infty} e^{-i\omega\tau_N} + \sum_{k=2}^{N} \left(\frac{k - k-1}{\tau_k - \tau_{k-1}}\right)\left(e^{-i\omega\tau_{k-1}} - e^{-i\omega\tau_k}\right)\right. \quad (1)$$

where $\dot{}_{\infty}$ is the slope of (τ) extrapolated to infinite time, τ is the lag time, τ_N is the Nth lag time, and 1 and N represent the first and last point of the oversampled (τ). The PCHIP function in MATLAB was used to perform oversampling. The complex modulus, $G^*(\omega) = G'(\omega) + iG''(\omega)$, was then determined from $\hat{}(\omega)$ as

$$^*(\omega) = \left(\frac{\kappa}{6\pi a}\right)\left(\frac{1}{i\omega\,\hat{}(\omega)} - 1\right), \qquad (2)$$

where a is the bead radius and κ is the trap stiffness. From G' and G'', the complex viscosity $\eta = (G'^2 + G''^2)^{1/2}/\omega$, and loss tangent $\tan\delta = G''/G'$ were also computed. All data shown in Fig. 3 are averages over 20 trials performed with different beads in different regions of the sample. Error bars represent the standard error obtained from the 20 trials.

To perform nonlinear OTM measurements, an optically trapped probe was displaced a distance of 10 μm through the composite at a constant speed of v = 10 μm s^{-1} using a nanopositioning piezoelectric stage (PDQ-250, Mad City Laboratories) to move the sample chamber relative to the trap. Following this 1 s strain phase, the trap is held fixed for 15 s while the probe relaxes back towards the center of the trap. The laser deflection is recorded at 20 kHz during both the strain and relaxation phases (Fig. 1(B) and (D)). The nonlinear force curves displayed in Fig. 4 and 5 are averages over two sets of 30 trials using 30 different probes at different locations in the sample chamber (see Fig. S6, ESI†). Error bars represent standard error across all trials. The actin concentration and strain rate were both chosen to be higher than the previously determined concentration and strain rate necessary for the onset of nonlinear mechanics.[37] In this regime, the probe pushes the network out of equilibrium, deforming and rearranging filaments, as we describe in the following sections.[56] Custom LabVIEW (National Instruments) and Matlab codes were used for all instrumentation control, data acquisition, and data analysis.

3 Results

Design of interpenetrating networks of actin and vimentin that mimic *in vivo* structures

To decipher the distinct contributions from actin and vimentin and the emergent interactions between the two filament types, we prepare composites with fixed total protein concentration of $c = c_V + c_A$ = 11.6 μM and varying molar fractions of actin $\phi_A = c_A/c$ and vimentin $\phi_V = 1 - \phi_A$ (Fig. 1(A)). Two-color confocal imaging experiments show that single-component networks (actin or vimentin only) and composites at all actin fractions ϕ_A comprise overlapping actin and vimentin filaments that are distributed across mesoscopic scales (200 μm) (Fig. S1(A), ESI†). To more closely examine possible heterogeneities throughout the sample chamber, we perform spatial image autocorrelation (SIA) analysis (see Methods) on single-channel images that comprise the composite projections shown in Fig. 1(A). Specifically, we compute a distinct intensity autocorrelation function $g(r)$ for each image of each network, which quantifies the extent to which two pixels separated by a distance r are correlated. We also split images into quadrants and compare $g(r)$ curves computed for each quadrant to assess in-plane heterogeneity. As shown in ESI,† Fig. S1(B), while both actin and vimentin display spread in the data, this spread is largely evenly distributed and appears to have no discernible dependence on filament type or composite composition.

We first aim to confirm that our composite preparation methods, which result in homogeneous interpenetrating networks of actin filaments and vimentin intermediate filaments, are physiologically relevant.[5] To demonstrate this relevance, we image actin filaments and vimentin IFs in mouse embryonic fibroblasts (mEF), as shown by the immunofluorescence images of an mEF, stained with spectrally-distinct fluorescent phalloidin and anti-vimentin antibodies that bind to actin and vimentin, respectively (Fig. 2(A)). While cellular actin and vimentin networks both appear to be heterogeneously distributed, there are distinct regions that comprise interpenetrating networks of actin and vimentin, qualitatively similar to those we observe *in vitro* (Fig. 1(A)).

To quantify the structural characteristics of these composite regions, we compute SIA autocorrelation functions $g(r)$, as described above, for actin and vimentin images. For simple homogeneous filament networks, $g(r)$ is expected to follow an exponential decay and the critical decay lengthscale can be understood as the characteristic structural correlation lengthscale ξ_g, which can serve as a proxy for mesh size (Fig. 2). As shown in Fig. 2(B), the functional form of the average $g(r)$ curves are similar for both filament types, but the vimentin structure appears to decay more weakly with increasing r. A single exponential is insufficient to capture either decay, which instead are well-described by a sum of two exponentials, $g(r) = c_1 e^{-r/\xi_{g,1}} + c_2 e^{-r/\xi_{g,2}}$, indicative of two structural lengthscales. The resulting small and large correlation lengths differ by an order of magnitude, with $\xi_{g,1} \simeq 0.41$ μm and $\xi_{g,2} \simeq 3.9$ μm for vimentin, which are similar to $\xi_{g,1} \simeq 0.43$ μm and $\xi_{g,2} \simeq 3.9$ μm for actin. However, the relative weight of the large lengthscale, *i.e.*, c_2, is larger for vimentin compared to actin (0.63 *vs.* 0.53) (Fig. S2(C), ESI†). To determine the degree of heterogeneity in each network, we fit the individual $g(r)$ curves(see Fig. S2(A) and (B), ESI†) that constitute the averages shown in Fig. 2(B) and extract corresponding parameters $\xi_{g,1}$,$\xi_{g,2}$,c_1,c_2 (see Fig. 2(C) and Fig. S2(C), ESI†). We observe a broader spread in the values for the larger lengthscales compared to smaller ones for both actin and vimentin, indicating that spatial heterogeneities emerge beyond the scale of several microns (Fig. 2(C)).

Evaluating the same $g(r)$ curves for single network images of our *in vitro* composites, we find qualitatively similar features as the *in vivo* measurements (Fig. 2(B)). Namely, vimentin networks appear to decay more weakly with increasing r (Fig. 2(D)), indicative of larger characteristic lengthscales compared to actin networks. Moreover, actin networks are well described by a double exponential with characteristic lengthscales comparable to *in vivo*, $\xi_{g,1} \simeq 0.87$ μm and $\xi_{g,2} \simeq 4.0$ μm, and similarly larger spread in $\xi_{g,2}$ values *versus* $\xi_{g,1}$ (Fig. 2(E)). While the vimentin autocorrelation is well-fit to a single rather than

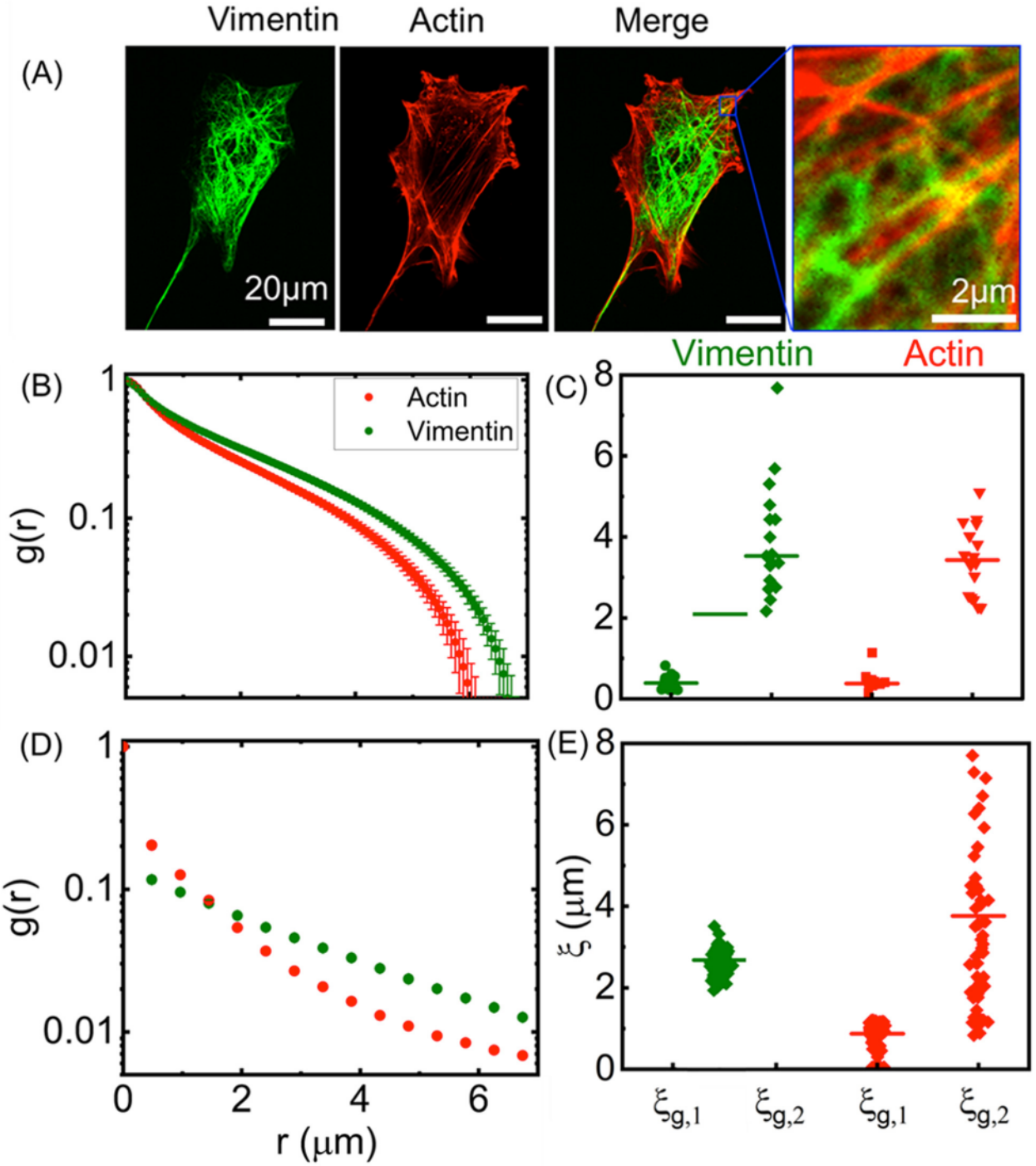

Fig. 2 Interpenetrating networks of actin and vimentin in cells have similar structural features as *in vitro* composites. (A) Immunofluorescence images of mouse embryonic fibroblasts (mEF) labeled for vimentin (left, green) and actin (red, middle left), with the two channels merged (middle right) and zoomed-in (right), respectively. (B)–(E) spatial image autocorrelation analysis is performed on images of composites in mEF cells (B) and (C) and compared to *in vitro* composite images (D) and (E). (B) Spatial image autocorrelation function $g(r)$ computed for the separate actin (red) and vimentin (green) channels of the *in vivo* fluorescence images shows a similar structural correlation for actin and vimentin that decays with increasing distance r. The characteristic distance r associated with the decay is a measure of the structural correlation length ξ_g for each filament network, shown in (C) for all images (circles) with the horizontal bars denoting the average $\xi_{g,A}$ and $\xi_{g,V}$. The data shows that both the average and spread in ξ_g values are modestly higher for vimentin compared to actin. (D) and (E) The same metrics extracted from cell images performed on fluorescence confocal images of *in vitro* composites (Fig. 1(A)) show (D) $g(r)$ curves and (E) ξ_g values for actin (red) and vimentin (green) have similar features to those measured in cells, with vimentin exhibiting slightly higher average $g(r)$ and ξ_g values and greater spread across different images. Data shown in (D) and (E) is an average over all data for ϕ_A = 0.25, 0.5, 0.75 composites.

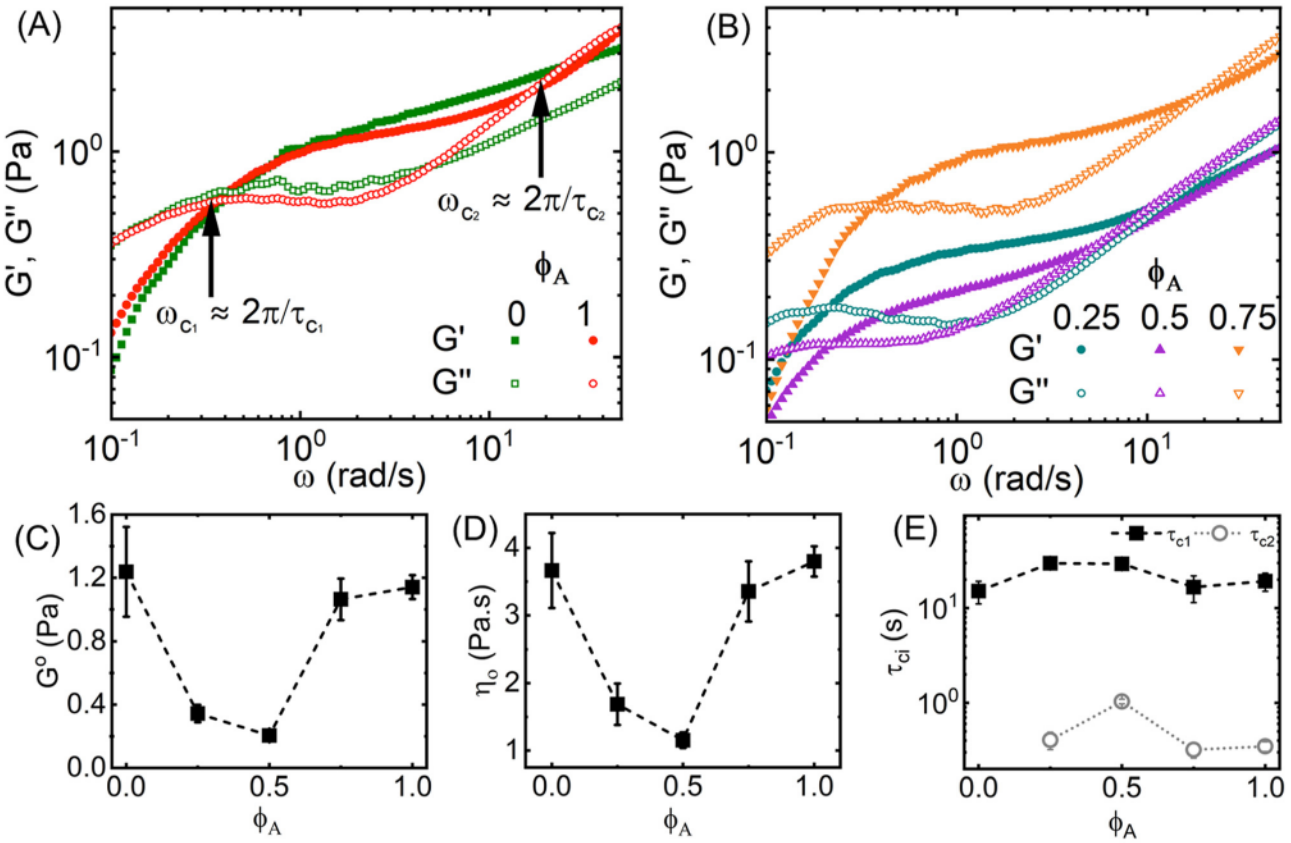

Fig. 3 Linear microrheological properties of actin–vimentin composites exhibit non-monotonic dependence on composite composition. (A) and (B) Linear frequency-dependent elastic (filled symbols) and viscous (open symbols) moduli, $G'(\omega)$ and $G''(\omega)$, for (A) single-component networks of actin filaments (ϕ_A = 1, red) and vimentin IFs (ϕ_A = 0, green) compared to (B) actin–vimentin composites with ϕ_A = 0.25 (dark cyan), 0.5 (purple) and 0.75 (orange). (C) Plateau modulus G^0 and (D) zero-shear viscosity η_0 display similar non-monotonic dependence on molar actin fraction ϕ_A, reaching minima at ϕ_A = 0.5. (E) The relaxation times τ_{c_i} determined from the frequencies ω_{c_i} at which $G'(\omega) = G''(\omega)$ *via* the relation $\tau_{c_i} = 2\pi\tau_{c_i}^{-1}$. Example slow and fast crossover frequencies, ω_{c_1} and ω_{c_2}, which correspond to the long and short relaxation times τ_{c_1} and τ_{c_2} are denoted in (A). Data shown is an average across 20 trials measured with different probes in different regions of the sample chamber. Error bars shown in (C)–(E) represent standard error across all 20 trials.

double exponential, the resulting lengthscale of $\xi_g \simeq 2.7$ μm (see Fig. S3 (left), ESI†) is quite close to the weighted average of the two *in vivo* vimentin lengthscales, $c_1 \quad \xi_{g,1} + c_2 \quad \xi_{g,2} \simeq$ 2.6 μm (Fig. 2(C)). These results demonstrate that our designed *in vitro* composites are structurally similar to *in vivo* networks, suggesting that the microscale mechanical properties we investigate may provide valuable new insights into cellular mechanics.

Actin–vimentin composites exhibit emergent non-monotonic viscoelastic properties depending on composite composition

We characterize the linear viscoelastic properties of the composites shown in Fig. 1(A) by analyzing the thermal fluctuations of optically trapped microspheres embedded in composites, as depicted in Fig. 1(B) and (C). Using the generalized Stokes–Einstein relationship (GSER), we determine the frequency-dependent linear elastic and viscous moduli, $G'(\omega)$ and $G''(\omega)$ for networks of either actin (ϕ_A = 1) or vimentin (ϕ_V = 0) (Fig. 3(A)) compared to composites (ϕ_A = 0.25, 0.5, 0.75) (Fig. 3(B)). We also calculate the crossover times, (τ_{c_1} & τ_{c_2}) (Fig. 3(E)), the frequency dependent shear viscosity, $\eta(\omega)$, and the loss tangent, tan δ (Methods, Fig. S4(B) and (C), ESI†).

We first observe that both the magnitude and frequency dependence of $G'(\omega)$ and $G''(\omega)$ are surprisingly similar for actin and vimentin networks despite the order of magnitude difference in their persistence lengths. Moreover, Fig. 2 suggests that the structural correlation of vimentin networks extends to larger lengthscales compared to actin, which we may expect to result in lower $G'(\omega)$ due to reduced entanglement density. We corroborate this modestly increased structural lengthscale using previously reported expressions for the mesh size of actin and vimentin networks with mass concentration c_A and c_V, $\xi_A \simeq 0.3c_A^{-1/2}$ and $\xi_V \simeq 0.42c_V^{-1/2}$, where c_A and c_V are in units of mg ml^{-1}, and the corresponding mesh sizes are in units of μm (see Fig. S5, ESI†).[16,66–71] From these expressions, we compute mesh sizes of $\xi_A \simeq 0.42$ μm and $\xi_V \simeq 0.52$ μm for actin and vimentin, respectively, which are comparable to $\xi_{g,1}$ values we report in Fig. 2.

The similarity between the two single-composite actin and vimentin networks is strongest at lower frequencies, where both networks exhibit terminal flow behavior, with $G''(\omega) \quad G'(\omega)$,

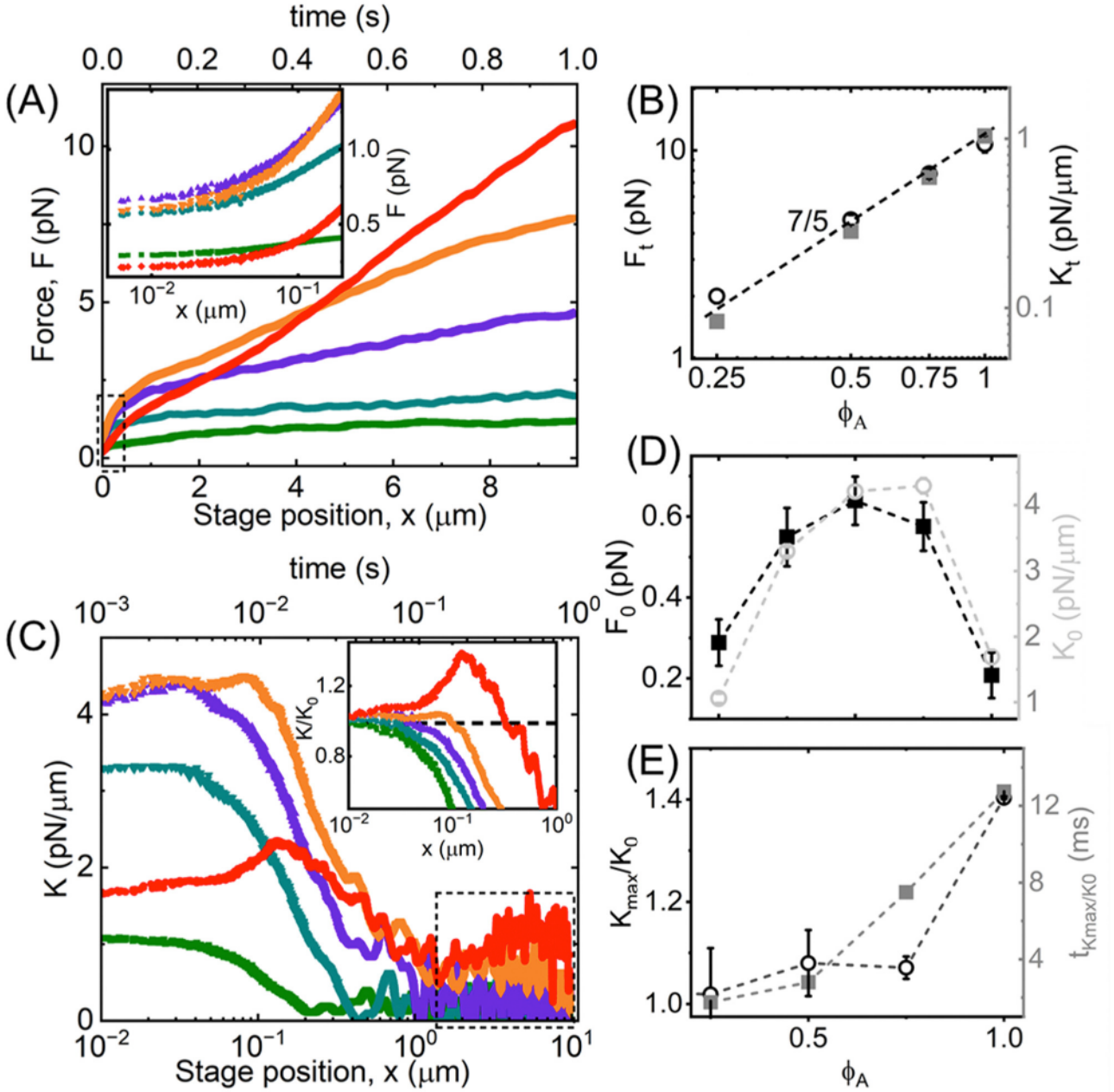

Fig. 4 Nonlinear microrheology of actin–vimentin composites manifests emergent stiffness not accessible in the linear regime that is suppressed at large strains. (A) The force exerted by composites with ϕ_A = 0 (green), 0.25 (dark cyan), 0.5 (purple), 0.75 (orange), and 1 (red) to resist the moving probe as it is displaced a distance x (bottom axis) over a time $t = x/v$ (top axis) at constant speed v = 10 μm s^{-1}. (Inset) Zoom-in of the small-x region denoted by dashed box to show the dependence of the initial force F_0 on ϕ_A. (B) Terminal force F_t (left black axis, open black circles) and stiffness K_t (right grey axis, filled grey squares) reached at the end of the strain phase as a function of ϕ_A. The dashed line denotes the predicted scaling for entangled actin networks G $c_A^{-7/5}$. (C) Stiffness $K(x) = dF/dx$ *versus* x (bottom axis) and t (top axis) computed from the data shown in (A). The dashed boxed-in region denotes the range of $K(x)$ values that are averaged to determine K_t values shown in (B). (Inset) Zoom-in of data normalized by the corresponding initial value K_0 for each composite shows the degree to which composites undergo stress stiffening (dK/dx 1) *versus* softening (dK/dx 1). The horizontal dashed line at $K = K_0$ highlights the degree of stress-stiffening (K/K_0 1) *versus* softening (K/K_0 1). (D) Initial force F_0 (left black axis, filled black squares) and stiffness K_0 (right grey axis, open grey circles) measured at the beginning of the strain (x = 0) both display non-monotonic dependence on ϕ_A. (E) Degree of stiffening K_{max}/K_0 (left black axis, open black circles) and the time over which composites exhibit stiffening $t_{K_{max}/K}$ (right grey axis, filled grey squares) increase with increasing ϕ_A. The error bars for F_t and F_0 were determined from the standard error of the OTM measurements of 30 trials (Fig. S6, ESI†), while bootstrapping over 1000 subsets was used for K_t, K_0, and K_{max}/K_0.

followed by a crossover to an elastic-dominated regime at ω_{c_1}, where $G'(\omega)$ becomes greater than $G''(\omega)$. This crossover frequency is a measure of the longest relaxation time of the network $\tau_{c_1} = 2\pi\omega_{c_1}^{-1}$ which is the disengagement time τ_D for entangled polymers. Namely, τ_D is the time over which an entangled polymer is able to diffuse out of its deformed entanglement tube and into a

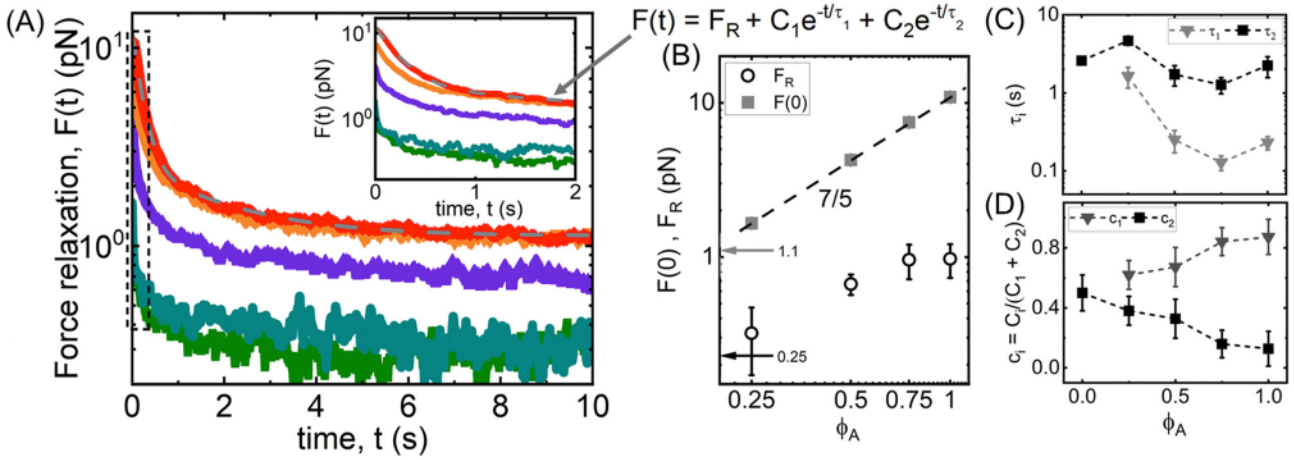

Fig. 5 Force relaxation of actin–vimentin composites following nonlinear straining is dictated primarily by entangled actin. (A) Relaxation of force F as a function of time t following the strain for composites with $\phi_A = 0$ (green), 0.25 (dark cyan), 0.5 (purple), 0.75 (orange) and 1 (red). (Inset) Zoom-in of small t region denoted by dashed box to show the dependence of the initial force F_0 on ϕ_A. (B) Force measured at the beginning ($F(0)$, grey squares) and end (F_R, black open circles) of the relaxation phase as a function of ϕ_A for ϕ_A 0 composites. Grey and black arrows and numbers indicate the values of $F(0)$ and F_R at $\phi_A = 0$. $F(0)$ is determined directly from the data and F_R is determined from fitting $F(t)$ to the function displayed above the plot: $F(t) = F_R + C_1e^{-t/\tau_1} + C_2e^{-t/\tau_2}$. The dashed line represents predicted scaling G $c_A^{1.4}$ for entangled actin networks. (C) Fast and slow relaxation times, τ_1 (grey triangles) and τ_2, (black squares), as functions of ϕ_A, determined from fitting the data in (A) to the function listed in (B). For $\phi_A = 0$ data, $\tau_1 \approx \tau_2$ and $C_1 \approx 0$, showing that it lacks the fast relaxation that composites with actin exhibit. (D) Fractional coefficients, $c_i = C_i/(C_1 + C_2)$ associated with the fast (c_1, grey triangles) and slow (c_2, black squares) relaxation modes as a function of ϕ_A. The error bars here were determined from the standard error of the OTM measurements of 30 trials.

pristine tube.[35,37,72] We measure similar values of $\tau_{c_1} \simeq 19$ s and 15 s for actin and vimentin networks, respectively. We also find comparable values for the elastic plateau modulus G^0 for the two networks, $G^0_A \simeq 1.1$ Pa and $G^0_V \simeq 1.2$ Pa which we determine by evaluating G' at the frequency at which the loss tangent is minimum (Fig. 3(C) and Fig. S4B, ESI†).[73,74]

Deviations between the two networks emerge at higher frequencies, $\omega \gtrsim 3$ rad s^{-1}, where the actin network exhibits a second crossover to a viscous-dominated regime at ω_{c_2}, a signature of entangled polymers at timescales below the entanglement time τ_e, where mechanics are dominated by single chains that do not feel the constraints of their neighbors.[72] The lack of a crossover for vimentin networks is suggestive of tighter constraints and extended timescales over which interactions with neighboring chains dominate the mechanics, ostensibly at odds with the larger mesh size of vimentin compared to actin.

Turning our attention to the composites, we find similar frequency dependence as single-component networks for all ϕ_A, including a low-frequency flow regime, a crossover at ω_{c_1}, and elastic plateau regime defined by a plateau modulus G^0 (Fig. 3(B)). Similar to actin networks, all composites also exhibit a high-frequency crossover at ω_{c_2} that is absent in the vimentin-only ($\phi_A = 0$) network. This result may indicate that the relaxation mechanism related to $\tau_{c_2} = 2\pi\omega_{c_2}^{-1}$ is a signature of the actin in the composites or that the mechanism preventing this crossover in $\phi_A = 0$ is disrupted or suppressed.

While the frequency dependence of $G'(\omega)$ and $G''(\omega)$ is similar for composites and single-component networks, their magnitudes are universally lower for composites. This effect can be seen clearly in Fig. 3(C) which shows a strong non-monotonic dependence of the plateau modulus G^0 on ϕ_A, with G^0 dropping by a factor of 6 from $G^0 \simeq 1.2$ Pa at $\phi_A = 0$ to 0.2 Pa at $\phi_A = 0.5$ followed by a increase back to 1.1 Pa at $\phi_A = 1$. We observe a very similar non-monotonic dependence of the zero-shear viscosity η_0, which we approximate as the complex viscosity η at the lowest frequency we measure (Fig. 3(D) and Fig. S4(C), ESI†).

Finally, we examine the ϕ_A-dependence of the slow and fast relaxation timescales, τ_{c_1} and τ_{c_2} determined from the respective crossover frequencies. We find weaker dependence on ϕ_A compared to the moduli magnitudes (Fig. 3(C) and (D)), particularly for the slower timescale, which we expect to be related to the disengagement time τ_D. The fast timescale τ_{c_2} shows a peak at $\phi_A = 0.5$, indicative of a longer time required for the onset of entanglement dynamics if we assume $\tau_{c_2} \simeq \tau_e$, a result that aligns with the corresponding minimum in G^0.

Our collective linear regime results suggest that composites have weaker constraints and are more easily able to dissipate local stresses compared to single-component networks. However, the similarity in the longest measured relaxation timescales across the composition space suggests that universal relaxation mechanisms may be at play. Moreover, our results are ostensibly at odds with previous bulk rheology experiments that report an increase in G^0 for composites *versus* vimentin-only composites,[18] or a monotonic decrease in G^0 with increasing ϕ_A.[16] We conjecture that these differences arise from variations in the filament concentrations we use compared to the previous bulk measurements, which may result in relatively increased mesh size and/or suppressed non-specific crosslinking for composites *versus* vimentin-only networks in our studies. Importantly, these distinctions also highlight the need for both bulk and microscale rheological measurements that probe mechanics at different spatiotemporal scales, and have different sensitivities to, *e.g.*,

varying mesh sizes, to understand the complex mechanical response of cytoskeleton composites.

Nonlinear straining induces emergent stiffness of actin–vimentin composites that is quenched at large strains

To determine the extent to which the behavior we observe in the linear regime holds when composites are subject to large nonlinear strains that push them out of equilibrium, we perform nonlinear constant rate OTM measurements (Fig. 1(B) and (D)). In each of these measurements, the same optically trapped probe used for linear OTM is displaced a distance x_{max} = 10 μm through the composite at constant speed v = 10 μm s^{-1}, after which the probe is held fixed for 15 s. We measure the force the composite exerts to resist the strain and the subsequent relaxation of the force as the probe is held fixed. In response to the strain, all networks exhibit a sharp rise in force, followed by a more shallow rise with increasing distance x, as shown in Fig. 4(A). For ϕ_A 0.5, the response force reaches a nearly strain-independent plateau, indicating a largely viscous terminal response. However, as ϕ_A increases, the large-strain response force becomes increasingly dependent on x (*i.e.*, the slope of $F(x)$ increases), a signature of increasing elasticity or stiffness. The magnitude of $F(x)$ likewise increases with ϕ_A, a dependence that we quantify by evaluating the terminal value of the force at the end of the strain $F_t = F(x$ = 10 μm) as a function of ϕ_A (Fig. 4(B)). We find that F_t follows power-law scaling F_t ϕ_A^{α} with scaling exponent $\alpha \simeq 1.4$ that aligns with the scaling of the shear modulus with concentration for entangled actin networks,[71,75,76] suggesting that actin dominates the long-time behavior in the nonlinear regime.

To shed further light on the extent to which elastic contributions to the stress response manifest at different lengthscales, we also evaluate the composite stiffness $K = dF/dx$ as a function of distance x and time $t = x/v$ (Fig. 4(C)). In the large strain limit ($x \gtrsim 2$ μm), K universally reaches a roughly constant value that increases with increasing ϕ_A. We find that this terminal value K_t follows similar power-law scaling as F_t (Fig. 4(B)), corroborating the dominant role that actin plays in persistent stiffness and elasticity of composites. Importantly, this monotonic power-law increase in F_t and K_t with ϕ_A is distinct from the non-monotonic dependence we observe in the linear regime, in which ϕ_A = 0 vimentin networks exhibited stronger elastic signatures than ϕ 0 composites.

We next examined the initial short-time behavior, which we expect to be largely dictated by elastic-like contributions due to the lack of available relaxation mechanisms to appreciably dissipate stress. As shown in the inset of Fig. 4(A), we observe a dependence on ϕ_A that is quite different than that of both the terminal nonlinear behavior as well as the linear viscoelasticity. Namely, the initial force F_0 is substantially larger for composites compared to single-component networks, in direct opposition to the non-monotonic trend we find for the linear regime metrics G^0 and η_0 which are minimized for composites (Fig. 3(C) and (D)). We observe similar non-monotonicity for initial stiffness K_0 (Fig. 4(C) and (D)), corroborating the emergence of enhanced elasticity in composites compared to single-component networks. This emergent behavior may suggest microscale interactions between actin and vimentin,[18] depletion-driven restructuring,[25] or increased poroelasticity,[12,77–80] ideas we explore further below. Closer examination of $K(x)$ also reveals modest stress stiffening, *i.e.*, dK/dx 1 for some composites before transitioning to softening dK/dx 0 to a final constant value K_t (Fig. 4(B)). While previous studies have found that vimentin promotes stress-stiffening in cytoskeletal compositess,[25,42–44] we do not find strain stiffening behavior of vimentin networks for the conditions used here, as shown in Fig. 4(C) inset, which shows the x-dependent degree of stiffening $K(x)/K_0$. The vimentin-only network exhibits no initial stiffening, and the maximum degree of stiffening K_{max}/K_0 as well as the time that the stiffening regime persists, namely the time at which K_{max}/K_0 reaches its maximum, t_{K_{max}/K_0}, increases monotonically with ϕ_A (Fig. 4(E)). This effect, qualitatively similar to the dependence of F_t and K_t, corroborates our understanding that the nonlinear response is dictated primarily by the actin filaments in the composites, which endow composites with stiffness and persistent elasticity for all but the shortest timescales.

Actin promotes both sustained elasticity and fast relaxation modes in actin–vimentin composites

The nonlinear strain response suggests that actin allows for more sustained elasticity, which we expect to result in reduced relaxation of force following strain as the actin fraction increases. To investigate this conjecture, we measure the time-dependent decay of the force $F(t)$ that each composite exerts on the trapped probe following cessation of the strain (Fig. 5(A)). We first note that the force at the onset of the relaxation phase, $F(0)$, increases with increasing ϕ_A (Fig. 5(A) inset) and displays the same power-law dependence as F_t and K_t (Fig. 4(B)), *i.e.*, $F(0)$ $\phi_A^{1.4}$ (Fig. 4(B)), as expected as they are measured in close succession, and further supporting the dominant role that actin plays in persistent stiffness.

We also evaluate the residual force maintained at the end of the relaxation phase F_R, which should equate to $F(0)$ and 0 for purely elastic and viscous materials, respectively. Namely, for a purely elastic material, there should be no force relaxation following the strain, such that $F(t) = F(0)$, while a purely viscous fluid would immediately relax all stress once the strain ceases ($F(t)$ 0). As shown in Fig. 5(B), F_R increases with increasing ϕ_A, suggestive of increased sustained elasticity, until ϕ_A = 0.75 at which point it saturates at 1 pN (10% of $F(0)$).

These results demonstrate that actin dictates the ability of composites to exhibit elastic memory following nonlinear straining, which suggests actin is more readily able to withstand large strains, as compared to vimentin, without entanglements being disrupted or filaments being forcibly rearranged. To determine the relaxation mechanisms underlying this behavior, we turn to the time-dependence of $F(t)$ *en route* from $F(0)$ to F_R (Fig. 5(A)). We find that in the absence of actin (ϕ_A = 0), the force relaxation can be described by a single exponential and offset F_R: $F(t) = Ce^{-t/\tau} + F_R$ with a characteristic decay time of $\tau \simeq 2.6$ s. However, all ϕ_A 0 composites require a sum of two exponentials, $F(t) = C_1e^{-t/\tau_1} + C_2e^{-t/\tau_2} + F_R$, to accurately

describe the force relaxation, similar to previous studies on actin networks and composites.[12,35,81]

The characteristic decay times τ_i and relative coefficients $c_i = C_i/(C_1 + C_2)$ provide measures of the relaxation times and the degree to which that associated relaxation mechanism contributes to the force relaxation (Fig. 5(C) and (D)). We first note that the decay time for the vimentin network is comparable to the τ_2 values measured for composites ($\tau \simeq \tau_2$), so we attribute the decay to the same mechanism. Further, the additional relaxation time that emerges when actin is present, τ_1, is faster than τ and generally comparable to τ_{c_2} values measured in the linear regime (Fig. 3(E)). The absence of τ_{c_2} for the vimentin-only network in the linear regime (Fig. 3(E)) is consistent with the lack of τ_1 in the nonlinear regime (Fig. 5(C)), suggesting that it is the same mechanism in both regimes that underlies the fast relaxation and that it is an actin relaxation mode. We also find the c_1 increases with increasing ϕ_A, providing further evidence for this phenomenon. As c_1 increases with ϕ_A, c_2 by the definition of c_i, decreases, reaching 0.2 for $\phi \geq 0.75$. This decrease mirrors the increase in F_R, indicating that it is the suppression of the slow relaxation mechanism, likely the disengagement time, that allows for sustained elasticity. Conversely, actin allows for fast relaxation, consistent with the relaxation of filament segments on the order of the confinement tube diameter, which occurs over the entanglement time τ_e. More flexible polymers, such as vimentin, are expected to have much faster entanglement times, which are beyond the resolution of our measurement.[18] Alternatively, intermittent crosslinking of vimentin chains would further speed up or altogether eliminate this fast mode. We elaborate on these possible mechanisms below.

4 Discussion

Our measurements have revealed stark differences between the dependence of composite composition on the mechanical properties of actin–vimentin networks in the linear regime *versus* the nonlinear regime, as well as at short and long timescales. The nearly opposite emergence of weaker *versus* stiffer response characteristics of composites as compared to single-component actin or vimentin networks, shown in Fig. 3 and 4, suggest that different relaxation mechanisms drive the response in the different regimes. More importantly, the non-monotonic dependence highlights the emergent mechanical properties that actin–vimentin composite designs afford that are not a simple sum of the two individual network properties, and may facilitate cellular processes that demand switchable and hierarchical mechanical properties, such as in migration, morphogenesis and division.[8–13]

To understand the mechanisms underlying these distinct responses, we first compare the relaxation times that we measure in linear (Fig. 3) and nonlinear (Fig. 4) regimes (Fig. 6(A)). The linear and nonlinear fast timescales, τ_1 and τ_{c_2}, which are absent in the vimentin-only ($\phi_A = 0$), are comparable across all ϕ_A values (Fig. 6(A)). As described above, τ_{c_2} for entangled polymers is a measure of the entanglement time τ_e which, for semiflexible polymers, is predicted to depend on the mesh size ξ and persistence length l_p as $\tau_e \simeq \varepsilon \xi^{16/5} l_p^{-1/5}$ where ε is the friction term which is expected to be 3 s μm^{-3} for actin.[33,82] We compute the ϕ_A-dependent mesh size of the composites ξ_c using the relation $\xi_c \approx (\xi_A^{-3} + \xi_V^{-3})^{-1/3}$ along with $\xi_A \simeq 0.3 c_A^{-1/2}$ and $\xi_V \simeq 0.42 c_V^{-1/2}$ (Fig. S5, ESI†).[12,16] From these expressions, we compute τ_e values for actin that range from 262 ms to 120 ms as ϕ_A increases from 0.25 to 1. The $\phi_A = 1$ value ($\tau_e \simeq 120$ ms) is comparable to our measured values of $\tau_1 = 230$ ms and $\tau_{c_2} \simeq 346$ ms, but the increase in these timescales with decreasing ϕ_A is substantially stronger than the predicted dependence assuming a mesh size ξ_c. However, if we consider that the actin network appears to dominate the nonlinear response at the end of the strain, we may also expect that the initial relaxation may be likewise dominated by the actin network. As such, if we instead use the mesh size of the actin network ξ_A in the predicted expression for τ_e, we compute values of $\tau_e \simeq 193$, 369, and 1119 ms for $\phi_A = 0.75$, 0.5, 0.25, which are comparable to the measured τ_1 values of 129 ms, 249 ms, 1631 ms. The linear regime fast relaxation timescale τ_{c_2} is also of the same order as τ_1 and τ_e for actin but exhibits a weaker and more non-monotonic dependence on ϕ_A, resembling the ϕ_A-dependence of ξ_c *versus* ξ_A.

Taken together, our results reveal that it is the entanglements between actin filaments that gives rise to the fast relaxation timescale in composites. While the presence of vimentin contributes to the mesh size that dictates the actin relaxation in the linear regime, the relaxation of vimentin itself does not appear to play a role. Moreover, in the nonlinear regime, the relevant confinement network appears to be that of the actin rather than the composite, suggestive of possible forces disentanglement of the vimentin from the actin at the leading edge of the probe.[83–85] This physical picture is consistent with the ostensibly negligible contribution of vimentin to the long-time nonlinear response (Fig. 4(A)) and evidence of forced de-threading in other composite systems.[84–86]

Turning to the slow relaxation timescales measured in the linear and nonlinear regimes, τ_{c_1} and τ_2, we find that both timescales display similar weak dependence on ϕ_A (Fig. 6(A)). However, τ_2 is generally an order of magnitude faster than τ_{c_1}. Insofar as we can understand this slow timescale as a measure of the disengagement time, τ_D, this faster relaxation in the nonlinear regime is consistent with several previously reported studies of actin networks and composites, in which τ_D was predicted and shown to be faster in the nonlinear regime due to tube dilation and/or entanglement hopping.[35,39,55] The former is a result of convective constraint release or forced disentanglement that decreases the local entanglement density and thus speeds up disengagement, while the latter is a process whereby an entangled polymer can hop from one cage to another when an entanglement is transiently disrupted.[35,40,87] These mechanisms are direct consequences of nonlinear straining and are largely inaccessible in the quiescent linear regime. The magnitude of τ_2 and its relative insensitivity to concentration is consistent with previous microrheology measurements on actin networks and composites, which were also shown to adopt these non-classical relaxation mechanisms.[12,35] Further, in the linear regime, τ_D for actin is predicted to be independent of

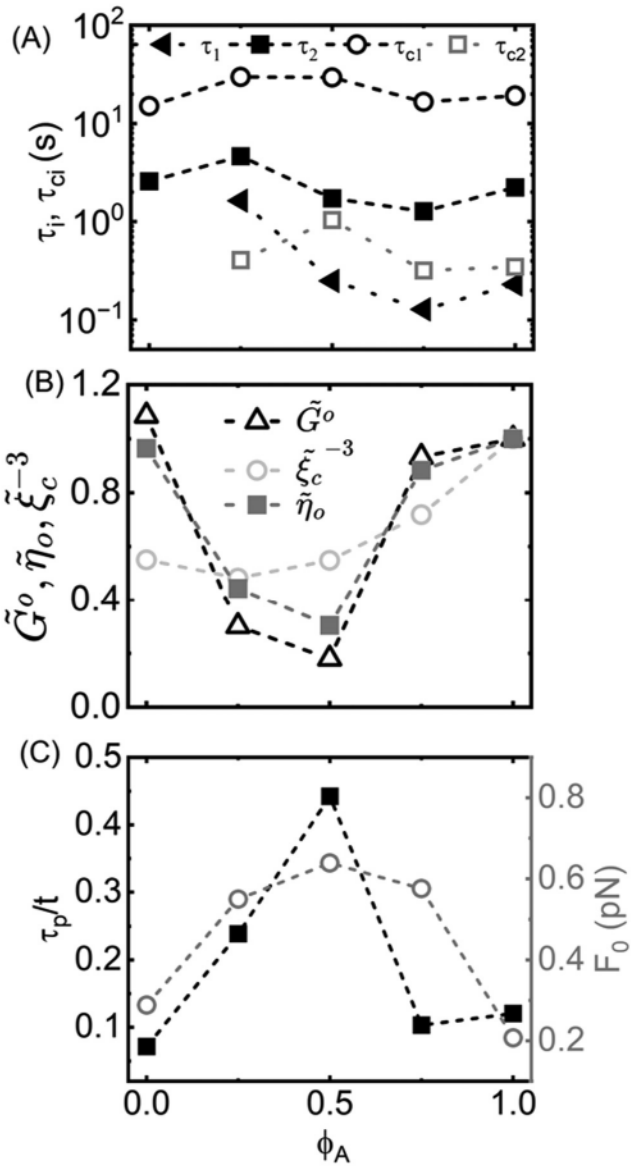

Fig. 6 Distinct emergent mechanics of actin–vimentin composites in linear and nonlinear regimes are sculpted by the interplay between actin entanglements, vimentin crosslinking, and poroelasticity. Various metrics and timescales measured in linear and nonlinear regimes *versus* actin fraction ϕ_A. (A) Relaxation timescales from linear (τ_{c_i}, open symbols) and nonlinear (τ_i, filled symbols) OTM measurements that correspond to fast (τ_{c_2}, open grey squares; τ_1, black triangles) and slow (τ_{c_1}, open black circles; τ_2, black squares) relaxation modes. (B) Non-monotonic ϕ_A-dependence of measured linear regime metrics, G^0 and η_0, and predicted composite mesh density ξ_c^{-3}, each scaled by their value at $\phi_A = 1$: $\tilde{G}^0$ (triangles), $\tilde{\eta}_0$ (squares) and $\tilde{\xi}_c^{-3}$ (circles). (C) The ratio of predicted poroelastic relaxation time τ_p to measurement time t (left black axis, black squares) and initial force F_0 measured during the nonlinear strain phase (right grey axis, grey circles) both display non-monotonic dependence on ϕ_A with maxima at $\phi_A = 0.5$.

concentration and scale as $\tau_D \sim L^3$,[33] consistent with the insensitivity of τ_{c_1} that we uncover.

Given the similar ϕ_A-dependence of the relaxation timescales in the linear and nonlinear regimes, coupled with the near opposite dependence of the magnitude of stress response metrics (*i.e.*, G^0, η_0, F_0) on ϕ_A, demands further discussion. In the linear regime, composites appear to be weaker than their single-component counterparts, as summarized in Fig. 6(B), which shows the plateau modulus and zero-shear viscosity, normalized by their $\phi_A = 1$ values, $\tilde{G}^0 = G^0/G^0(\phi_A = 1)$ and $\tilde{\eta}_0 = \eta_0/\eta_0(\phi_A = 1)$. Both quantities follow very similar profiles, reaching minima of ~ 0.2 and ~ 0.3 at $\phi_A = 0.5$. This signature of weaker confinement suggests that the composite mesh size may also exhibit a non-monotonic dependence on ϕ_A. Namely, the moduli should scale roughly with the density of the mesh ξ_c^{-3} that sets the confinement. Comparing $\tilde{\xi}_c^{-3}$ with $\tilde{G}_0$ and $\tilde{\eta}_0$ (Fig. 6(B)), we find that ξ_c^{-3} indeed follows a non-monotonic dependence on ϕ_A but its minimum is reached at, $\phi_A = 0.25$ rather than $\phi_A = 0.5$ and the $\phi_A = 0$ value is nearly 2-fold lower than that for $\phi_A = 1$ (actin only) and only modestly larger than the minimum at $\phi_A = 0.25$. Thus, the decreasing mesh density may explain the drop in moduli values as ϕ_A decreases from 1 to 0.5, but the subsequent rise in values as ϕ_A goes to 0 is substantially more pronounced than the mesh density can account for. We rationalize that the larger than expected value for the vimentin-only network is a result of VIF crosslinking, mediated by divalent cations, as reported in previous studies.[21,22,46–48] Moreover, previous studies have suggested that introducing actin into vimentin networks may serve to block binding sites and disrupt VIF crosslinking,[9] which aligns with the large drop in G^0 and η_0 that we observe between $\phi_A = 0$ and 0.25. While previous studies have also indicated potential crosslinking of actin to vimentin,[18] we find no evidence of this interaction, which may be due to the lower filament concentration and ionic strengths we examine compared to this previous study. Crosslinking of vimentin in the absence of actin would also greatly reduce or eliminate τ_e, which our data indicate, as crosslinking enhances confinement and reduces the timescale over which filaments can freely diffuse. However, if the crosslinks were long-lived then we may also expect the disappearance of the long relaxation timescale τ_D and terminal flow regime, which we do not observe. This effect indicates that crosslinks are transient, as previously suggested,[22] such that the filaments can still exhibit flow-like behavior on long timescales.

The transient and weak nature of the crosslinks likely play an important role in the different responses we observe in the nonlinear regime. The dominant role that actin plays in the nonlinear response (Fig. 4(A)), along with the very weak terminal stiffness K_t and force F_t measured for vimentin networks compared to composites and actin networks (Fig. 6(B)), indicates that the nonlinear strain is able to easily disrupt the crosslinks, as previously reported,[22] so they do not contribute to the nonlinear stress response. However, this effect is seemingly at odds with the initial response behavior in which composites exhibit more pronounced stiffness and resistance compared to single-component networks, rather than the monotonic increase with increasing ϕ_A that we see for the longer time response features.

To understand these distinct trends, we consider that disruption of vimentin crosslinks is likely to only have a noticeable impact at lengthscales beyond the length between crosslinks, which we can estimate as the vimentin mesh size if we assume that all vimentin crossings contain non-steric linkages. The predicted vimentin mesh size ranges from $\xi_V \simeq 0.51$ μm

to 1 μm for ϕ_A = 0 to 0.75. The average vimentin correlation length measured from confocal images is similarly $\xi_{g,V} \approx 1$ μm. Examination of Fig. 4(A) indeed reveals that the distance x at which $F(x)$ for the actin network becomes comparable to and exceeds that of the composites occurs at $x \approx 1$ μm.

The question remains as to what physical mechanism underlies the emergent stiffness and resistive force F_0 of composites at lengthscales below 1 μm (Fig. 6(C)), which is distinct from both the linear response and large-lengthscale nonlinear response. At these very fast timescales (~1 ms, which are faster than most of the available relaxation modes of the filaments, *i.e.*, τ_e, the poroelasticity of the network can contribute to its response to a fast-moving probe.[12,77–80] Namely, the hydrodynamic drag from a probe of diameter d displacing the solvent of viscosity η_s that pervades the network can contribute to the force response at timescales comparable to or lower than the draining time of the fluid, which sets the poroelastic relaxation time $\tau_p \simeq d x \eta / 2G^0 \xi^2$. At timescales above τ_p the deformation of the network dominates the response and the hydrodynamic effects of poroelasticity can be neglected. Using our measured G^0 values and computed ξ_c values for each ϕ_A, along with $x = vt$ where v = 10 μm s^{-1}, we evaluate the ratio of the poroelastic timescale to measurement timescale, $\tau_p/t \simeq d v \eta / 2G^0 \xi_c^2$, as a function of ϕ_A (Fig. 6(C)). The larger this ratio, the more effect that poroelastic resistance (*i.e.*, slow fluid draining) will have on the initial force response. As shown in Fig. 6(C), τ_p/t follows a similar non-monotonic trend as the initial force response F_0, reaching a maximum at ϕ_A = 0.5, suggesting that it is, in fact, the increased poroelastic relaxation timescales of the composites that give rise the emergent increase in initial force response for composites compared to single-component networks. Perhaps counterintuitively, this effect is coupled to the corresponding reduced elastic modulus of composites in the linear regime, demonstrated by the inverse relation between τ_p and G^0. While the mesh size is larger for composites, which lowers the poroelastic ratio *via* the relation $\tau_p \sim \xi^{-2}$, ξ_c drops by less than 30% while G^0 increases 6-fold so the increased mesh size has less of an effect.

5 Conclusion

In conclusion, our suite of optical tweezers microrheology measurements on composites of varying molar fractions of semiflexible actin filaments and flexible vimentin intermediate filaments reveal novel emergent stress response features that are elegantly sculpted by the spatiotemporal scales of the strain. The complex interplay between varying filament stiffness, mesh size, crosslinking, and poroelasticity as the relative molar fractions of actin and vimentin gives rise to seemingly opposite non-monotonic dependence of the response on ϕ_A in linear and nonlinear measurements. This switchable rheology likely plays an important role in cellular processes, such as morphogenesis, adhesion and migration, and may be harnessed for designing multifunctional materials such as soft filtration and sequestration devices. Moreover, our results suggest that transient crosslinking of vimentin dominates the linear viscoelastic response of vimentin-rich composites, while the relative ease with which they can be disrupted hampers the extent to which vimentin fingerprints on the nonlinear response. These weak and switchable non-steric interactions, reminiscent of hydrogen bonding, likely contribute to the broad range and versatility of the mechanical processes that vimentin has been suggested to facilitate in cells.

Notably, vimentin has typically been considered to be responsible for the stress-stiffening behavior of cells due its increased extensibility and resistance to buckling, as compared to actin and microtubules. Our results challenge this view, revealing that actin–VIF composites exhibit reduced linear viscoelasticity compared to single-component networks. Moreover, the nonlinear response yields an opposite effect, with composites exhibiting enhanced stiffness compared to single component networks due to slower poroelastic relaxation timescales. Our analyses suggest that transient crosslinking of VIFs plays a principal role in the complex scale-dependent mechanical response we measure. Our findings further highlight the importance of separation of relaxation timescales between VIFs and actin, to emergent hierarchical mechanical properties. The ability of cells to tune their response based on the spatiotemporal scale of the strain, is critical to processes such as morphogenesis and adhesion. More generally, our results reinforce the important effect of scale on mechanical properties, in particular for composites with a broad range of characteristic length and time scales. Indeed, the hierarchical mechanical properties of the composite cytoskeleton have been recognized as playing an essential role in its ability to modulate myriad mechanical processes and properties with a finite number of building blocks.

Beyond implications our work has for cellular mechanics, we expect our reported response features and underlying mechanisms to be generalizable to a broad range of polymer composites that have species with varying relaxation timescales and transient interactions. Similar emergent nonlinear stiffening has been reported in actin–DNA composites;[88,89] and emergent filament mobility, analogous to decreased viscosity, has been reported in actin–microtubule composites.[12] Non-monotonic dependence of viscoelasticity on actin crosslinking on has also been reported in actin–microtubule composites.[90] As in our study, emergence was rationalized in these previous works as arising from competition between increased stiffness and mesh size as well as a spectrum of separable relaxation timescales, including reptation, poroelasticity, crosslinker unbinding, and bending.

Our future work will explore the role of vimentin crosslinking by modulating divalent cation concentration and using truncated VIFs that lack the tail domain that is expected to mediate crosslinking.[21,22] We will also vary the overall protein concentration, which may tip the scales towards actin–vimentin crosslinking and stiffening behavior in vimentin networks by increasing polymer overlap and entanglement density.

Author contributions

JP and RS performed experiments; AP provided guidance on experiments and materials, helped interpret data, and reviewed

and edited the manuscript; RMRA provided guidance on experiments and analysis, interpreted data, and wrote the manuscript; BJG designed and guided experiments, analyzed and interpreted data, and wrote the manuscript.

Data availability

The authors confirm that the data supporting the findings of this study are available within the article.

Conflicts of interest

The authors declare no conflict of interest.

Acknowledgements

We thank Bobby Carroll for supplying vimentin samples and Karthik Peddireddy for assistance with OTM acquisition and analysis software. This research was funded by Bucknell University (BJG), NSF DMREF 2119663 and NIH R15GM123420 to RMRA, and NSF CMMI 2238600 and NIH R35GM142963 to AP.

References

1 M. L. Gardel, K. E. Kasza, C. P. Brangwynne, J. Liu and D. A. Weitz, *Methods Cell Biol.*, 2008, **89**, 487–519.
2 L. Blanchoin, R. Boujemaa-Paterski, C. Sykes and J. Plastino, *Physiol. Rev.*, 2014, **94**, 235–263.
3 T. Svitkina, *Cold Spring Harbor Perspect. Biol.*, 2018, **10**, a018267.
4 G. M. Cooper, *The cell: a molecular approach*, 2000, vol. 2.
5 H. Wu, Y. Shen, S. Sivagurunathan, M. S. Weber, S. A. Adam, J. H. Shin, J. J. Fredberg, O. Medalia, R. Goldman and D. A. Weitz, *Proc. Natl. Acad. Sci. U. S. A.*, 2022, **119**, e2115217119.
6 T.-H. Chang, H.-D. Huang, W.-K. Ong, Y.-J. Fu, O. K. Lee, S. Chien and J. H. Ho, *Biomaterials*, 2014, **35**, 3934–3944.
7 A. E. Patteson, A. Vahabikashi, K. Pogoda, S. A. Adam, K. Mandal, M. Kittisopikul, S. Sivagurunathan, A. Goldman, R. D. Goldman and P. A. Janmey, *J. Cell Biol.*, 2019, **218**, 4079–4092.
8 F. Huber, A. Boire, M. P. López and G. H. Koenderink, *Curr. Opin. Cell Biol.*, 2015, **32**, 39–47.
9 M. H. Jensen, E. J. Morris, R. D. Goldman and D. A. Weitz, *Bioarchitecture*, 2014, **4**, 138–143.
10 C. Lorenz and S. Köster, *Biophys. Rev.*, 2022, **3**, 031304.
11 T. D. Pollard and R. D. Goldman, *Cold Spring Harbor Perspect. Biol.*, 2018, **10**, a030288.
12 S. N. Ricketts, J. L. Ross and R. M. Robertson-Anderson, *Biophys. J.*, 2018, **115**, 1055–1067.
13 S. N. Ricketts, M. L. Francis, L. Farhadi, M. J. Rust, M. Das, J. L. Ross and R. M. Robertson-Anderson, *Sci. Rep.*, 2019, **9**, 1–12.
14 Y.-C. Lin, G. H. Koenderink, F. C. MacKintosh and D. A. Weitz, *Soft Matter*, 2011, **7**, 902–906.
15 M. Das and F. MacKintosh, *Phys. Rev. E: Stat., Nonlinear, Soft Matter Phys.*, 2011, **84**, 061906.
16 T. Golde, C. Huster, M. Glaser, T. Händler, H. Herrmann, J. A. Käs and J. Schnauß, *Soft Matter*, 2018, **14**, 7970–7978.
17 A. E. Patteson, R. J. Carroll, D. V. Iwamoto and P. A. Janmey, *Phys. Biol.*, 2020, **18**, 011001.
18 O. Esue, A. A. Carson, Y. Tseng and D. Wirtz, *J. Biol. Chem.*, 2006, **281**, 30393–30399.
19 P. A. Janmey, S. Hvidt, J. Peetermans, J. Lamb, J. D. Ferry and T. P. Stossel, *Biochemistry*, 1988, **27**, 8218–8227.
20 M. Schopferer, H. Bär, B. Hochstein, S. Sharma, N. Mücke, H. Herrmann and N. Willenbacher, *J. Mol. Biol.*, 2009, **388**, 133–143.
21 Y.-C. Lin, C. P. Broedersz, A. C. Rowat, T. Wedig, H. Herrmann, F. C. MacKintosh and D. A. Weitz, *J. Mol. Biol.*, 2010, **399**, 637–644.
22 A. Aufderhorst-Roberts and G. H. Koenderink, *Soft Matter*, 2019, **15**, 7127–7136.
23 F. Alisafaei, K. Mandal, R. Saldanha, M. Swoger, H. Yang, X. Shi, M. Guo, H. Hehnly, C. A. Castañeda and P. A. Janmey, *et al.*, *Commun. Biol.*, 2024, **7**, 658.
24 P. A. Janmey, U. Euteneuer, P. Traub and M. Schliwa, *J. Cell Biol.*, 1991, **113**, 155–160.
25 A. V. Schepers, C. Lorenz, P. Nietmann, A. Janshoff, S. Klumpp and S. Köster, *Proc. Natl. Acad. Sci. U. S. A.*, 2021, **118**, e2102026118.
26 J. Block, V. Schroeder, P. Pawelzyk, N. Willenbacher and S. Köster, *Biochim. Biophys. Acta, Mol. Cell Res.*, 2015, **1853**, 3053–3064.
27 H. Herrmann and U. Aebi, *Cold Spring Harbor Perspect. Biol.*, 2016, **8**, a018242.
28 K. Pogoda, F. Byfield, P. Deptuła, M. Ciesluk, Ł. Suprewicz, K. Skłodowski, J. L. Shivers, A. Van Oosten, K. Cruz and E. Tarasovetc, *et al.*, *Nano Lett.*, 2022, **22**, 4725–4732.
29 R. Insall, *Curr. Biol.*, 2021, **31**, R496–R498.
30 M. L. Gardel, I. C. Schneider, Y. Aratyn-Schaus and C. M. Waterman, *Annu. Rev. Cell Dev. Biol.*, 2010, **26**, 315.
31 O. Lieleg, K. Schmoller, M. Claessens and A. Bausch, *Biophys. J.*, 2009, **96**, 4725–4732.
32 P.-G. De Gennes, *Scaling concepts in polymer physics*, Cornell University Press, 1979.
33 H. Isambert and A. Maggs, *Macromolecules*, 1996, **29**, 1036–1040.
34 J. Xu, Y. Tseng and D. Wirtz, *J. Biol. Chem.*, 2000, **275**, 35886–35892.
35 B. Gurmessa, R. Fitzpatrick, T. T. Falzone and R. M. Robertson-Anderson, *Macromolecules*, 2016, 3948–3955.
36 C. Semmrich, R. J. Larsen and A. R. Bausch, *Soft Matter*, 2008, **4**, 1675–1680.
37 T. T. Falzone, S. Blair and R. M. Robertson-Anderson, *Soft Matter*, 2015, **11**, 4418–4423.
38 T. T. Falzone and R. M. Robertson-Anderson, *ACS Macro Lett.*, 2015, **4**, 1194–1199.
39 D. M. Sussman and K. S. Schweizer, *Macromolecules*, 2012, **45**, 3270–3284.
40 D. M. Sussman and K. S. Schweizer, *Macromolecules*, 2013, **46**, 5684–5693.
41 Q. D. Tran, V. Sorichetti, G. Pehau-Arnaudet, M. Lenz and C. Leduc, *Phys. Rev. X*, 2023, **13**, 011014.

42 D. A. Fletcher and R. D. Mullins, *Nature*, 2010, **463**, 485–492.
43 M. B. McCormick, P. Kouklis, A. Syder and E. Fuchs, *J. Cell Biol.*, 1993, **122**, 395–407.
44 B. Alberts, A. Johnson, J. Lewis, M. Raff, K. Roberts and P. Walter, *Molecular Biology of the Cell*, Garland Science, 4th edn, 2002.
45 K. M. Heidemann, A. Sharma, F. Rehfeldt, C. F. Schmidt and M. Wardetzky, *Soft Matter*, 2015, **11**, 343–354.
46 Y.-C. Lin, N. Y. Yao, C. P. Broedersz, H. Herrmann, F. C. MacKintosh and D. A. Weitz, *Phys. Rev. Lett.*, 2010, **104**, 058101.
47 S. Köster, Y.-C. Lin, H. Herrmann and D. A. Weitz, *Soft Matter*, 2010, **6**, 1910–1914.
48 H. Wu, Y. Shen, D. Wang, H. Herrmann, R. D. Goldman and D. A. Weitz, *Biophys. J.*, 2020, **119**, 55–64.
49 I. Elbalasy, N. Wilharm, E. Herchenhahn, R. Konieczny, S. G. Mayr and J. Schnauß, *Polymers*, 2022, **14**, 614.
50 H. Lopez-Menendez and L. Gonzalez-Torres, *J. Mech. Phys. Solids*, 2019, **127**, 208–220.
51 Y. Shen, H. Wu, P. J. Lu, D. Wang, M. Shayegan, H. Li, W. Shi, Z. Wang, L.-H. Cai and J. Xia, *et al.*, *Phys. Rev. Lett.*, 2021, **127**, 108101.
52 Y. Shen, *Biophys. J.*, 2020, **118**, 440a.
53 R. Bucki, D. V. Iwamoto, X. Shi, K. E. Kerr, F. J. Byfield, Ł. Suprewicz, K. Skłodowski, J. Sutaria, P. Misiak and A. Z. Wilczewska, *et al.*, *J. Biol. Chem.*, 2023, **299**, 8.
54 R. Kirmse, Z. Qin, C. M. Weinert, A. Hoenger, M. J. Buehler and L. Kreplak, *PLoS One*, 2010, **5**, e12115.
55 C. D. Chapman and R. M. Robertson-Anderson, *Phys. Rev. Lett.*, 2014, **113**, 098303.
56 R. M. Robertson-Anderson, *Optical tweezers microrheology: from the basics to advanced techniques and applications*, 2018.
57 S. Winheim, A. R. Hieb, M. Silbermann, E.-M. Surmann, T. Wedig, H. Herrmann, J. Langowski and N. Mücke, *PLoS One*, 2011, **6**, e19202.
58 B. J. Gurmessa, M. J. Rust, M. Das, J. L. Ross and R. M. Robertson-Anderson, *Front. Phys.*, 2021, **667**, 760340.
59 C. Robertson and S. C. George, *J. Biomed. Opt.*, 2012, **17**, 080801.
60 M. E. Dwyer, R. M. Robertson-Anderson and B. J. Gurmessa, *Polymers*, 2022, **14**, 4980.
61 G. Lee, G. Leech, M. J. Rust, M. Das, R. J. McGorty, J. L. Ross and R. M. Robertson-Anderson, *Sci. Adv.*, 2021, **7**, eabe4334.
62 G. Lee, G. Leech, P. Lwin, J. Michel, C. Currie, M. J. Rust, J. L. Ross, R. J. McGorty, M. Das and R. M. Robertson-Anderson, *Soft Matter*, 2021, **17**, 10765–10776.
63 R. M. Robertson-Anderson, *Trends Biochem. Sci.*, 2024, DOI: 10.1016/j.tibs.2024.04.009.
64 R. Brau, J. Ferrer, H. Lee, C. Castro, B. Tam, P. Tarsa, P. Matsudaira, M. Boyce, R. Kamm and M. Lang, *J. Opt. A: Pure Appl. Opt.*, 2007, **9**, S103.
65 M. Tassieri, R. Evans, R. L. Warren, N. J. Bailey and J. M. Cooper, *New J. Phys.*, 2012, **14**, 115032.
66 F. Gittes, B. Schnurr, P. Olmsted, F. C. MacKintosh and C. F. Schmidt, *Phys. Rev. Lett.*, 1997, **79**, 3286.
67 D. C. Morse, *Phys. Rev. E: Stat. Phys., Plasmas, Fluids, Relat. Interdiscip. Top.*, 1998, **58**, R1237.
68 T. Gisler and D. A. Weitz, *Phys. Rev. Lett.*, 1999, **82**, 1606.
69 T. G. Mason, T. Gisler, K. Kroy, E. Frey and D. Weitz, *J. Rheol.*, 2000, **44**, 917–928.
70 C. F. Schmidt, M. Baermann, G. Isenberg and E. Sackmann, *Macromolecules*, 1989, **22**, 3638–3649.
71 M. Gardel, M. Valentine, J. C. Crocker, A. Bausch and D. Weitz, *Phys. Rev. Lett.*, 2003, **91**, 158302.
72 M. Doi and S. F. Edwards, *The theory of polymer dynamics*, Oxford University Press, 1988, vol. 73.
73 Y. Luan, O. Lieleg, B. Wagner and A. R. Bausch, *Biophys. J.*, 2008, **94**, 688–693.
74 F. G. Schmidt, B. Hinner and E. Sackmann, *Phys. Rev. E: Stat. Phys., Plasmas, Fluids, Relat. Interdiscip. Top.*, 2000, **61**, 5646.
75 B. Hinner, M. Tempel, E. Sackmann, K. Kroy and E. Frey, *Phys. Rev. Lett.*, 1998, **81**, 2614.
76 A. Palmer, T. G. Mason, J. Xu, S. C. Kuo and D. Wirtz, *Biophys. J.*, 1999, **76**, 1063–1071.
77 Y.-C. Lin, G. H. Koenderink, F. C. MacKintosh and D. A. Weitz, *Macromolecules*, 2007, **40**, 7714–7720.
78 E. Moeendarbary, L. Valon, M. Fritzsche, A. R. Harris, D. A. Moulding, A. J. Thrasher, E. Stride, L. Mahadevan and G. T. Charras, *Nat. Mater.*, 2013, **12**, 253–261.
79 Z. I. Kalcioglu, R. Mahmoodian, Y. Hu, Z. Suo and K. J. Van Vliet, *Soft Matter*, 2012, **8**, 3393–3398.
80 Y. Hu, X. Zhao, J. J. Vlassak and Z. Suo, *Appl. Phys. Lett.*, 2010, **96**, 12.
81 B. Gurmessa, S. Ricketts and R. M. Robertson-Anderson, *Biophys. J.*, 2017, 1540–1550.
82 J. Käs, H. Strey, J. Tang, D. Finger, R. Ezzell, E. Sackmann and P. Janmey, *Biophys. J.*, 1996, **70**, 609.
83 J. Uhde, W. Feneberg, N. Ter-Oganessian, E. Sackmann and A. Boulbitch, *Phys. Rev. Lett.*, 2005, **94**, 198102.
84 K. R. Peddireddy, R. Clairmont, P. Neill, R. McGorty and R. M. Robertson-Anderson, *Nat. Commun.*, 2022, **13**, 5180.
85 K. R. Peddireddy, M. Lee, Y. Zhou, S. Adalbert, S. Anderson, C. M. Schroeder and R. M. Robertson-Anderson, *Soft Matter*, 2020, **16**, 152–161.
86 K. R. Peddireddy, M. Lee, C. M. Schroeder and R. M. Robertson-Anderson, *Phys. Rev. Res.*, 2020, **2**, 023213.
87 S. J. Anderson, C. Matsuda, J. Garamella, K. R. Peddireddy, R. M. Robertson-Anderson and R. McGorty, *Biomacromolecules*, 2019, **20**, 4380–4388.
88 R. Fitzpatrick, D. Michieletto, K. R. Peddireddy, C. Hauer, C. Kyrillos, B. J. Gurmessa and R. M. Robertson-Anderson, *Phys. Rev. Lett.*, 2018, **121**, 257801.
89 D. Michieletto, R. Fitzpatrick and R. M. Robertson-Anderson, *Soft Matter*, 2019, **15**, 6703–6717.
90 M. L. Francis, S. N. Ricketts, L. Farhadi, M. J. Rush, M. Das, J. L. Ross and R. M. Robertson-Anderson, *Soft Matter*, 2019, **15**, 9056–9065.